

Virasoro Generators in the Fibonacci Model Tensor Network — Tackling Finite Size Effects

Xiangdong Zeng,^{1,2} Ruoshui Wang,³ Ce Shen,^{1,2} and Ling-Yan Hung^{1,2,4,5,*}

¹*State Key Laboratory of Surface Physics, Fudan University, Shanghai 200433, China*

²*Department of Physics and Center for Field Theory and Particle Physics, Fudan University, Shanghai 200433, China*

³*Cornell University, Ithaca, New York 14853, USA*

⁴*Institute for Nanoelectronic devices and Quantum computing, Fudan University, Shanghai 200433, China*

⁵*Yau Mathematical Sciences Center, Tsinghua University, Beijing 100084, China*

(Dated: December 7, 2022)

In this paper, we extend the method implementing Virasoro operators in a tensor network we proposed in [1] and test it on the Fibonacci model, which is known to suffer from far more finite size effects. To pick up the “seed” state that would flow to the stress tensor in the thermodynamic limit, we make use of the topological idempotent that projects the transfer matrix to the trivial sector. Combined with an optimization method, the seed state can be identified. We demonstrate that the descendant states in the Fibonacci model can be correctly generated with this approximate stress tensor, giving further evidence that the method applies more generally.

I. INTRODUCTION

There is a lot of progress in the last few years in recovering data of a continuous field theory from lattice models in a controlled numerical setting making use of tensor networks [2–12]. Particularly, in the case of 2D conformal field theories (CFT), there is by now a lot of work on extracting the CFT spectra from the tensor networks. More recently, there are works developing methodologies to understand how conformal and other (continuous) symmetries are realized on the tensor networks [4, 8, 9, 13, 14].

These methods mainly focus on constructing discrete operators that act on a 1D lattice Hilbert space. However, they are not immediately applicable when we work on tensor networks that directly reconstruct the 2D partition functions. Frequently, we combine with tensor renormalization algorithms so that individual tensors building up the tensor network representation of the partition function are known only numerically, making it technically difficult to recover the Hamiltonian picture by taking the time evolution $\Delta t \rightarrow 0$ limit. In [1], we proposed a method to implement the Virasoro symmetries from the intuitive picture that the insertion of Virasoro operators is equivalent to the insertion of the stress tensor with appropriate weight around a closed loop. We implement stress tensor insertion by solving for the eigenstates of a small cylinder. By the state-operator correspondence, these eigenstates represent a small disk with the stress tensor inserted at its center. These small disks are then inserted around a large disk to extract Virasoro descendants of the state corresponding to the large disk. We demonstrated this method in the case of the Ising model and found that this naive method appears to work quite well.

The Ising model is known to be very special and suffers from less severe finite size effects. In this paper, we would like to inspect our proposal in other models where finite size effects are more severe. Particularly, we will consider the \mathbb{Z}_3 parafermion CFT, which can be obtained by giving appropriate boundary conditions to the Fibonacci Levin–Wen topological order. Here, the spectrum of a cylinder of intermediate sizes would still look quite far from the actual CFT spectrum. This however does not mean that we cannot extract anything useful out of it. As the cylinder gets bigger, the spectrum would approach that of the CFT, and there is a sense of continuity in the process of solving for eigenstates for cylinders of larger and larger sizes. It is well known that one can record the respective eigenvalues as cylinder size grows and this allows one to extract the asymptotic eigenvalues numerically with only cylinders of finite size. See for example [2, 7, 15, 16].

In this paper, we will explain how we can pick up the eigenstate of a cylinder that would flow towards the stress tensor. A technical complication arises here, since the stress tensor is a fairly excited state in the spectrum, unlike in the case of the Ising model (we briefly reviewed the calculation of Ising CFT spectrum in Appendix A), making it more cumbersome to identify the eigenstate that would eventually flow to the actual stress tensor. To help identify the stress tensor, we make use of the projector constructed in [2, 7, 15–17]. It can be constructed using the tube algebra method [18, 19], and can project transfer matrix into sectors with definite topological charges. In the case of the stress tensor, it belongs to the trivial sector. Since the topological charges are explicit down to the smallest lattice scale in the lattice realization based on the string-net model, the eigenstate that could possibly flow to the stress tensor in the thermodynamic limit should still be found in the topologically trivial sector. The projector thus helps to remove a large number of states from other sectors. With the help of the projector, we identify the “seed” stress tensor

* lyhung@fudan.edu.cn

Using such a tensor unit, we would like to construct the transfer matrix M — which is the discrete version of the path-integral of the CFT on a cylinder, the latter is reviewed in the appendix. Consider putting the basic tensor units together to form a ring:

$$\begin{aligned} \tilde{M}_{i_1 i_2 \dots i_n, j_1 j_2 \dots j_n} &= \sum_{\substack{i_1, i_2, \dots, i_n \\ j_1, j_2, \dots, j_n}} \prod_{\alpha=1}^n A_{i_\alpha j_\alpha j_{\alpha+1} i_{\alpha+1}} \\ &= \text{Diagram (9)} \end{aligned} \quad (9)$$

Different from the square lattice case (e.g. typically in the 2D Ising model), the indices of A_{ijkl} are placed at corners, so they should be connected carefully in the particular order and orientation during contractions. Furthermore, the above cylinder \tilde{M} is still not sufficient for a correct transfer matrix that is equal only to the exponentiation of the Hermitian. If we stack these cylinders row by row, the result will be a slanted cylinder and an additional phase will appear in the final spectrum. By putting two copies of cylinders with opposite orientations together, i.e. taking

$$M = \tilde{M} \tilde{M}^\dagger, \quad (10)$$

this phase can be removed.

As discussed in [1, 3], we can obtain the CFT spectrum by diagonalizing $T \cdot M$, where T is the translation operator. In the tensor network representation, T is simply given by shifting the lattice by one site:

$$T_{i_1 i_2 \dots i_n, j_1 j_2 \dots j_n} = \text{Diagram (11)} \quad (11)$$

III. CFT SPECTRUM OF FIBONACCI STRING-NET

A. Calculation

In the thermodynamic limit, the Fibonacci string-net (critical hard-hexagon model with $c = 4/5$) approaches the \mathbb{Z}_3 parafermion CFT, but not all topological defects of the continuum CFT ($\mathbb{Z}_3 \otimes \text{Fib}$) have matrix product operator (MPO) representations in this specific lattice model [7]. Therefore, to get the “empty” torus partition function without non-trivial topological defects, we have to look at a transfer matrix with $n = 3k$ sites. Correspondingly, we should use a 3-site translation operator (or T^3) as well.

The memory consumption for the above construction grows exponentially with cylinder size n . To practically perform the calculation, we need to store the trans-

fer matrix in the form of LinearOperator [22]. The basic idea is that retaining the whole tremendous matrix in the memory is unnecessary; instead, what we need is the matrix-vector multiplication of this transfer matrix as an “operator”. Due to the nature of tensor network representation, it’s not difficult to construct such a multiplication function. The details of the implementation are given in Appendix B.

B. Spectrum of the transfer matrix

The spectrum data are listed in Table I. Fibonacci model suffers from significant finite size effects and hence only cylinders with size $n \gtrsim 20$ can give a relatively accurate result. For small cylinders, some excitation states may not even show up among the low-lying states. In principle, we can separate different states based on their scaling dimensions and conformal states. But due to the finite size effects, not only are the eigenvalues far from their limiting CFT values, there are ubiquitous issues with level-crossing — some supposedly highly excited states in the thermodynamic limit pick up small eigenvalues when the cylinder is small, which makes it difficult to distinguish them. Here, we assume that the scaling dimensions Δ will approach the thermodynamic limiting values as a power-law $\Delta = An^{-k} + B$ [23], and we optimize the fitting results by selecting eigenstates of the small cylinder that actually flow to the desired CFT conformal states (i.e. choose the point nearest to the fitting curve). The “ ∞ ” column in Table I is obtained by extrapolating cylinder size $n \rightarrow \infty$ (equal to B in the power-law formula). To estimate the scaling dimension more accurately, we can fix the identity state $|\phi_1\rangle$ and state $|\phi_T\rangle$ corresponding to the stress tensor such that $\Delta_1 = 0$ and $\Delta_T = 2$:

$$\Delta_\alpha = \frac{2}{\log \lambda_T - \log \lambda_I} (\log \lambda_\alpha - \log \lambda_I), \quad (12)$$

where λ_α are the corresponding eigenvalues. The results are listed in the “Rescaled” column and plotted in Figure 1.

When there are many states mingled together, however, the optimization procedure is troublesome and may not be guaranteed to find the correct state. To simplify the task, we make use of the projector mentioned in the introduction. It was constructed in [7, 15, 17, 21, 24], which would project the transfer matrix to a sub-space with definite topological charge. For the stress tensor, it belongs to the trivial sector, whose corresponding projector can be readily employed. In the next section, we will describe the construction of the needed idempotent in detail.

Spin \ Size	9	12	15	18	21	24	27	∞	Rescaled	Exact
0	0.0	0.0	0.0	0.0	0.0	0.0	0.0	0.0	0.0	0
0 ^a	0.112899	0.113952	0.114474	0.114769	0.114950	0.115070	0.115152	0.115519 (8)	0.1299 (6)	$\frac{2}{15}$
0	0.722756	0.709100	0.703083	0.699890	0.697989	0.696765	0.695931	0.69313 (5)	0.779 (4)	$\frac{4}{5}$
± 1	0.785553	0.817591	0.841528	0.859630	0.873686	0.884880	0.893989	1.11 (2)	1.25 (3)	$1 + \frac{2}{15}$
± 1	1.594955	1.346025	1.242196	1.184631	1.147942	1.122492	1.103796	1.051 (7)	1.18 (1)	$1 + \frac{2}{15}$
0^a	1.290074	1.222673	1.196184	1.182805	1.175050	1.170137	1.166820	1.1584 (6)	1.302 (6)	$\frac{4}{3}$
± 1	1.147427	1.222649	1.274342	1.312081	1.340887	1.363620	1.382029	1.66 (1)	1.87 (1)	$1 + \frac{4}{5}$
± 1	3.221770	2.490495	2.169235	2.016147	1.925379	1.865017	1.821876	1.703 (6)	1.91 (1)	$1 + \frac{4}{5}$
± 2	2.727358^b	2.139950	1.967143	1.887302	1.842910	1.815429	1.797149	1.779 (9)	2.00 (1)	2
± 2	1.032723 ^b	1.178227	1.276463	1.348394	1.403716	1.447739	1.483672	2.023 (5)	2.27 (1)	$2 + \frac{2}{15}$
± 2	- ^b	1.430687	1.484488	1.527193	1.561317	1.589035	1.611935	2.24 (7)	2.52 (9)	$2 + \frac{2}{15}$

^a There is a 2-fold degeneracy in these levels.

^b For $n = 9$ cylinder, the transfer matrix is not large enough, so some high-level descendants may not show up; at the same time, spin ± 2 will degenerate to ± 1 .

TABLE I. Fibonacci spectrum from transfer matrices of different sizes. Vacuum state and its descendants (marked with bold blue) are obtained by diagonalizing the transfer matrix with idempotents, see section III C. The cylinder sizes are from 9 to 27 and are extrapolated to infinity, with data listed in the “ ∞ ” column.

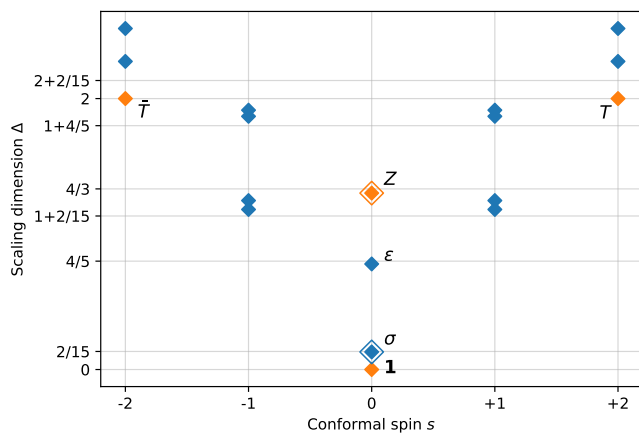


FIG. 1. Fibonacci spectrum corresponding to the cylinder transfer matrix of size $n \rightarrow \infty$. “ \blacklozenge ” indicates that there is a 2-fold degeneracy. The values have been rescaled so that $\Delta_{\mathbf{1}} = 0$ and $\Delta_T = 2$. Primary states are labeled with their corresponding operators, with conformal dimensions $h_{\mathbf{1}} = 0$, $h_{\sigma} = 1/15$, $h_{\epsilon} = 2/5$, $h_Z = 2/3$, $h_X = 7/5$ and $h_Y = 3$, respectively (states corresponding to X and Y are higher and they are not considered in our calculation). The CFT partition function is then $Z = |\chi_{\mathbf{1}} + \chi_Y|^2 + |\chi_{\epsilon} + \chi_X|^2 + 2|\chi_{\sigma}|^2 + 2|\chi_Z|^2$ [7]. The states that lie within the sub-space corresponding to the trivial sector $|\chi_{\mathbf{1}} + \chi_Y|^2$ are drawn in orange.

C. Topological Projectors

In the PEPS representation of the string-net models, each type of anyons of the topological model has a corresponding string operator. Their construction is related to the so-called Ocneanu’s tube algebra. Each type of anyon in the topological model corresponds to a topolog-

ical sector of the CFT — i.e. the families of primaries in the CFT can be organized into different topological sectors, each corresponding to an anyon of the topological model. Each string operator constructed in the topological model behaves as a projector that can project the CFT transfer matrix on a cylinder down to a sub-space containing states in this corresponding topological sector. Since we are particularly interested in obtaining the stress tensor, which belongs to the trivial sector in the topological model, we need the corresponding string operator. These operators take the form of matrix product operators (MPO) which have been systematically constructed in [7, 15, 17, 21, 24], and they are often referred to as the *idempotents*. We will review the needed ingredients below.

The tensor unit of such MPO is given by

$$\begin{array}{c}
 \begin{array}{c}
 \alpha \quad i \quad \delta \\
 \begin{array}{c}
 \text{---} \text{---} \text{---} \\
 \text{---} \text{---} \text{---} \\
 \text{---} \text{---} \text{---} \\
 \beta \quad i \quad \gamma
 \end{array}
 \end{array}
 \end{array}
 j = (d_{\alpha} d_{\beta} d_{\gamma} d_{\delta})^{\frac{1}{4}} G_{j\alpha\delta}^{\beta i \gamma},
 \end{array}
 \tag{13}$$

$$\begin{array}{c}
 \begin{array}{c}
 \alpha \quad i \quad \delta \\
 \begin{array}{c}
 \text{---} \text{---} \text{---} \\
 \text{---} \text{---} \text{---} \\
 \text{---} \text{---} \text{---} \\
 \beta \quad i \quad \gamma \\
 \quad \quad k
 \end{array}
 \end{array}
 \end{array}
 j = (d_{\alpha} d_{\beta} d_{\gamma} d_{\delta} d_i d_j d_k)^{\frac{1}{4}} G_{ij\alpha}^{k\beta\delta} G_{kj\delta}^{i\gamma\beta},$$

where G is a normalized and symmetric version of the

tetrahedron:

$$G_{ijk}^{abc} = \frac{1}{\sqrt{d_j d_c}} [F_b^{aik}]_{jc} = \frac{1}{\sqrt{d_a d_b d_c d_i d_j d_k}} \begin{array}{c} j \\ \triangle \\ i \\ k \\ a \\ b \\ c \end{array}. \quad (14)$$

For the cylinder transfer matrix of size n , the tube algebra basis is then given by a chain of $n-1$ orange tensors with a red one connected at the end (virtual legs to be contracted are omitted here):

$$\mathcal{T}_{ab}^c = a \text{---} \tau \text{---} \tau \text{---} \tau \text{---} \dots \text{---} \tau \text{---} b \text{---} c. \quad (15)$$

In general, the idempotents are linear combinations of these basis tensors, and the calculation of their coefficients can be found in Appendix C of [21]. Here, our aim is to identify the stress tensor which is the descendant of the vacuum state, so we need to use the idempotent projecting to the trivial sector. This is given by

$$\mathcal{P}_1 = \frac{1}{\sqrt{5}} \left(\frac{1}{\phi} \mathcal{T}_{11}^1 + \sqrt{\phi} \mathcal{T}_{\tau 1}^{\tau} \right). \quad (16)$$

Then it can be stacked to the transfer matrix (9) with translation operator (11). In Figure 1, the states that lie within the sub-space preserved by \mathcal{P}_1 are drawn in orange. The stress tensor T lies within this trivial sector, with many other intervening states with similar conformal dimensions removed. This allows us to recover the correct seed state that flows to the stress tensor.

IV. VIRASORO OPERATOR

Our method for constructing the Virasoro operator in lattice models is inspired by the success of “discrete holomorphicity”, a substantial subject reviewed for example in [25]. The basic idea is that a lattice version of contour integral can be approximated by discretely inserting operators along the intended path. In [1] we made the following proposal to implement Virasoro operators in a tensor network. We take the following definitions of the Virasoro operators in the continuous theory

$$L_n \sim \sum_{j=1}^N e^{ij n \frac{2\pi}{N}} T(j), \quad \bar{L}_n \sim \sum_{j=1}^N e^{-ij n \frac{2\pi}{N}} \bar{T}(j). \quad (17)$$

and take them seriously in a tensor network, by replacing the operator insertion at a point by the state we solved from the transfer matrix above at the vertex labeled j . Here, $T(j)$ and $\bar{T}(j)$ are eigenstates of the cylinder transfer matrix of finite size we found in previous sections. With the help of idempotents and optimization, they

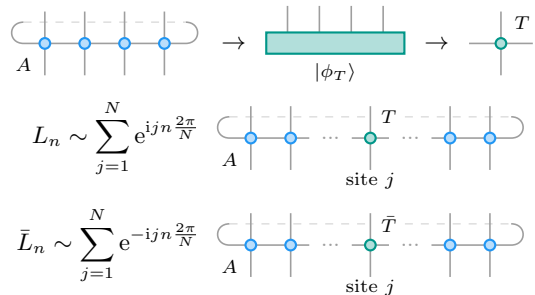


FIG. 2. Tensor network implementation of equation (17). Eigenstate $|\phi_T\rangle$ corresponding to the stress tensor is solved from the cylinder transfer matrix. It’s reshaped to a 4-leg tensor and then inserted into a new cylinder to construct the Virasoro operators.

are deemed to flow towards the actual CFT states corresponding to the stress tensor in the thermodynamic limit. The insertion procedure is depicted in Figure 2.

Since the cylinder’s size have to be $n = 3k$ for the Fibonacci case, we can’t directly insert the stress tensor T and \bar{T} into the new cylinder as it requires a 4-leg unit. Instead, we need to first reshape it into a triangle and then pad with “empty” triangle tensors equation (7) to obtain a square one, analogous to the tensor constructed in equation (8):

$$\begin{array}{c} i_1 \text{---} i_2 \text{---} i_3 \text{---} \dots \text{---} i_{n=3k} \text{---} \dots \end{array} = \begin{array}{c} \dots i_{2k+2} \dots \\ \triangle \\ i_2 \dots i_{k+2} \\ \dots \\ i_{k+1} \end{array} \rightarrow \begin{array}{c} \dots \\ \triangle \\ \dots \\ \triangle \\ \dots \end{array}. \quad (18)$$

Note that the contraction only involves the corner degrees of freedom. For the other sites of the new cylinder, we can build them in the same way. To make the contraction more efficient, however, we can block $k \times k$ square tensors in equation (8) as the unit equivalently.

In our calculation, we take cylinder size $n = 12, 15$ and 18 to find the eigenstates corresponding to the stress tensor. They are reshaped and padded into 4-leg tensor units with bond dimension $\chi = 2^{n/3}$. Then we use these tensor units as well as the blocking sites to form a new cylinder for obtaining the Virasoro operator. In principle, the size of the new cylinder N can be chosen arbitrarily. But due to the limit of memory resource, we have to take an $N = 3$ cylinder (equivalent to the n -site cylinder with bond dimension $\chi = 2$) for the calculation of the stress tensor in reality. We check their validity by applying these operators to low-energy eigenstates (same from size N cylinder) and see if they will be correctly raised or

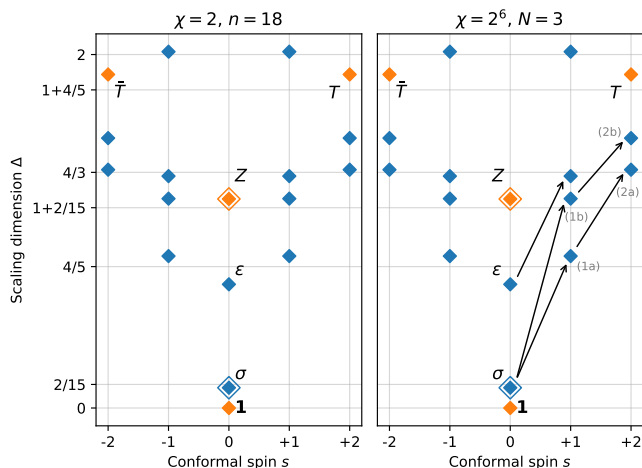


FIG. 3. We use the cylinder of size $n = 18$ to solve for the stress tensor (left). T and \bar{T} are used to build the Virasoro operators L_n and \bar{L}_n in a new cylinder of size $N = 3$ and bond dimension $\chi = 2^{n/3}$. The actions of L_{-1} are illustrated by the arrows as an example (right). The states labeled (1a)/(1b) and (2a)/(2b) should be degenerate at the CFT limit but are split here due to the finite size effect (cf. Figure 1). Note that to be consistent with the data in Appendix C, the scaling dimensions shown here are *not* rescaled.

lowered into certain levels. We show the actions of L_{-1} in Figure 3 and more numerical details can be found in Appendix C.

V. CONCLUSIONS

In this paper, we inspect our proposal of implementing Virasoro symmetry in a tensor network in a more

elaborate lattice model than the Ising model. Particularly, we worked with the Fibonacci model, which is known to suffer from more severe finite size effects. The method that we have proposed continues to work reasonably well — although in this case, to extract the stress tensor from a relatively small transfer matrix tiling a small cylinder, we need to make use of the method of the idempotent, to project out states with different topological charges. Paired with the optimization procedure which fits the eigenvalues in a power law as it approaches the thermodynamic limit, we can isolate the appropriate “seed” state that would flow to the stress tensor. We show that using a seed state to construct Virasoro operator still produces reasonably accurate descendants in a cylinder that is marred by finite size effects. This complements our earlier work, giving further evidence with an improved algorithm for reconstructing Virasoro symmetry in a more general tensor network.

ACKNOWLEDGMENTS

LYH acknowledges the support of NSFC (Grant No. 11922502, 11875111) and the Shanghai Municipal Science and Technology Major Project (Shanghai Grant No. 2019SHZDZX01), and Perimeter Institute for hospitality as a part of the Emmy Noether Fellowship Programme. We are particularly grateful to Prof. Frank Verstraete and Robijn Vanhove for multiple correspondences, explaining in detail the methodologies they employed in their beautiful series of papers. We also thank Lin Chen, Jiaqi Lou, Bingxin Lao and Xinyang Yu for useful discussions and comments.

-
- [1] R. Wang, X. Zeng, C. Shen, and L.-Y. Hung, Virasoro and Kac–Moody algebra in generic tensor network representations of two-dimensional critical lattice partition functions, *Phys. Rev. B* **106**, 115116 (2022), arXiv:2205.04500.
 - [2] G. Evenbly and G. Vidal, Local scale transformations on the lattice with tensor network renormalization, *Phys. Rev. Lett.* **116**, 040401 (2016), arXiv:1510.00689.
 - [3] M. Hauru, G. Evenbly, W. W. Ho, D. Gaiotto, and G. Vidal, Topological conformal defects with tensor networks, *Phys. Rev. B* **94**, 115125 (2016), arXiv:1512.03846.
 - [4] A. Milsted and G. Vidal, Extraction of conformal data in critical quantum spin chains using the Koo–Saleur formula, *Phys. Rev. B* **96**, 245105 (2017), arXiv:1706.01436.
 - [5] S. Yang, Z.-C. Gu, and X.-G. Wen, Loop optimization for tensor network renormalization, *Phys. Rev. Lett.* **118**, 110504 (2017), arXiv:1512.04938.
 - [6] M. Bal, M. Mariën, J. Haegeman, and F. Verstraete, Renormalization group flows of hamiltonians using tensor networks, *Phys. Rev. Lett.* **118**, 250602 (2017), arXiv:1703.00365.
 - [7] R. Vanhove, M. Bal, D. J. Williamson, N. Bultinck, J. Haegeman, and F. Verstraete, Mapping topological to conformal field theories through strange correlators, *Phys. Rev. Lett.* **121**, 177203 (2018), arXiv:1801.05959.
 - [8] Y. Zou, A. Milsted, and G. Vidal, Conformal data and renormalization group flow in critical quantum spin chains using periodic uniform matrix product states, *Phys. Rev. Lett.* **121**, 230402 (2018), arXiv:1710.05397.
 - [9] Y. Zou, A. Milsted, and G. Vidal, Conformal fields and operator product expansion in critical quantum spin chains, *Phys. Rev. Lett.* **124**, 040604 (2020), arXiv:1901.06439.
 - [10] Y. Zou and G. Vidal, Emergence of conformal symmetry in quantum spin chains: Antiperiodic boundary conditions and supersymmetry, *Phys. Rev. B* **101**, 045132 (2020), arXiv:1907.10704.
 - [11] T.-C. Huang, Y.-H. Lin, K. Ohmori, Y. Tachikawa, and M. Tezuka, Numerical evidence for a Haagerup conformal field theory, *Phys. Rev. Lett.* **128**, 231603 (2022), arXiv:2107.10704.

- 2110.03008.
- [12] R. Vanhove, L. Lootens, M. Van Damme, R. Wolf, T. J. Osborne, J. Haegeman, and F. Verstraete, Critical lattice model for a Haagerup conformal field theory, *Phys. Rev. Lett.* **128**, 231602 (2022), [arXiv:2110.03532](#).
- [13] W. Koo and H. Saleur, Representations of the Virasoro algebra from lattice models, *Nucl. Phys. B* **426**, 459 (1994), [arXiv:hep-th/9312156](#).
- [14] R. Wang, Y. Zou, and G. Vidal, Emergence of Kac-Moody symmetry in critical quantum spin chains, *Phys. Rev. B* **106**, 115111 (2022), [arXiv:2206.01656](#).
- [15] D. J. Williamson, N. Bultinck, and F. Verstraete, Symmetry-enriched topological order in tensor networks: Defects, gauging and anyon condensation, arXiv preprint (2017), [arXiv:1711.07982](#).
- [16] L. Lootens, R. Vanhove, J. Haegeman, and F. Verstraete, Galois conjugated tensor fusion categories and nonunitary conformal field theory, *Phys. Rev. Lett.* **124**, 120601 (2020), [arXiv:1902.11241](#).
- [17] D. Aasen, P. Fendley, and R. S. Mong, Topological defects on the lattice: dualities and degeneracies, arXiv preprint (2020), [arXiv:2008.08598](#).
- [18] D. E. Evans and Y. Kawahigashi, On Ocneanu's theory of asymptotic inclusions for subfactors, topological quantum field theories and quantum doubles, *International journal of mathematics* **6**, 205 (1995).
- [19] D. E. Evans, Y. Kawahigashi, *et al.*, *Quantum symmetries on operator algebras*, Vol. 147 (Clarendon Press Oxford, 1998).
- [20] O. Buerschaper, M. Aguado, and G. Vidal, Explicit tensor network representation for the ground states of string-net models, *Phys. Rev. B* **79**, 085119 (2009), [arXiv:0809.2393](#).
- [21] N. Bultinck, M. Mariën, D. Williamson, M. Şahinoğlu, J. Haegeman, and F. Verstraete, Anyons and matrix product operator algebras, *Ann. Phys.* **378**, 183 (2017), [arXiv:1511.08090](#).
- [22] P. Virtanen, R. Gommers, T. E. Oliphant, M. Haberland, T. Reddy, D. Cournapeau, E. Burovski, P. Peterson, W. Weckesser, J. Bright, S. J. van der Walt, M. Brett, J. Wilson, K. J. Millman, N. Mayorov, A. R. J. Nelson, E. Jones, R. Kern, E. Larson, C. J. Carey, Í. Polat, Y. Feng, E. W. Moore, J. VanderPlas, D. Laxalde, J. Perktold, R. Cimrman, I. Henriksen, E. A. Quintero, C. R. Harris, A. M. Archibald, A. H. Ribeiro, F. Pedregosa, P. van Mulbregt, and SciPy 1.0 Contributors, SciPy 1.0: Fundamental algorithms for scientific computing in python, *Nat. Methods* **17**, 261 (2020).
- [23] The power-law is used empirically and is not necessarily the only form. Other models, e.g. exponential model $\Delta = A \exp(-kn) + B$ can be applied here as well.
- [24] L. Lootens, R. Vanhove, and F. Verstraete, Cardy states, defect lines and chiral operators of coset CFTs on the lattice, arXiv preprint (2019), [arXiv:1907.02520](#).
- [25] J. Cardy, Discrete holomorphicity at two-dimensional critical points, *J. Stat. Phys.* **137**, 814 (2009), [arXiv:0907.4070](#).

Appendix A: Ising model

Anyon types of the 2D critical Ising model on square lattice are $\mathbf{1}$, σ and ψ , with quantum dimension $d_{\mathbf{1}} = d_{\psi} = 1$, $d_{\sigma} = \sqrt{2}$. Non-trivial fusion rules and F -symbols are

$$\begin{aligned} \sigma \times \sigma &= \mathbf{1} + \psi, & \sigma \times \psi &= \psi \times \sigma = \sigma, & \psi \times \psi &= \mathbf{1}; \\ F_{\sigma}^{\sigma\sigma\sigma} &= \frac{1}{\sqrt{2}} \begin{pmatrix} 1 & 1 \\ 1 & -1 \end{pmatrix}, & [F_{\sigma}^{\psi\sigma\psi}]_{\sigma\sigma} &= [F_{\psi}^{\sigma\psi\sigma}]_{\sigma\sigma} = -1. \end{aligned} \quad (\text{A1})$$

We can then write the tetrahedra and triangle tensors as follows:

$$\begin{aligned} \begin{array}{c} \mathbf{1} \\ \sigma \quad \sigma \\ \sigma \quad \sigma \\ \mathbf{1} \end{array} &= (d_{\mathbf{1}} d_{\sigma} d_{\sigma})^{-\frac{1}{4}} (d_{\mathbf{1}} d_{\sigma} d_{\sigma})^{-\frac{1}{3}} \begin{array}{c} \mathbf{1} \quad \sigma \\ \sigma \quad \sigma \\ \sigma \quad \mathbf{1} \end{array} = 2^{-\frac{1}{12}}, \\ \begin{array}{c} \psi \\ \sigma \quad \sigma \\ \sigma \quad \sigma \\ \mathbf{1} \end{array} &= (d_{\mathbf{1}} d_{\sigma} d_{\sigma})^{-\frac{1}{4}} (d_{\sigma} d_{\sigma} d_{\psi})^{-\frac{1}{3}} \begin{array}{c} \mathbf{1} \quad \sigma \\ \sigma \quad \sigma \\ \sigma \quad \psi \end{array} = 2^{-\frac{1}{12}}, \\ \begin{array}{c} \mathbf{1} \\ \sigma \quad \sigma \\ \sigma \quad \sigma \\ \psi \end{array} &= (d_{\sigma} d_{\sigma} d_{\psi})^{-\frac{1}{4}} (d_{\mathbf{1}} d_{\sigma} d_{\sigma})^{-\frac{1}{3}} \begin{array}{c} \psi \quad \sigma \\ \sigma \quad \sigma \\ \sigma \quad \mathbf{1} \end{array} = 2^{-\frac{1}{12}}, \\ \begin{array}{c} \psi \\ \sigma \quad \sigma \\ \sigma \quad \sigma \\ \psi \end{array} &= (d_{\sigma} d_{\sigma} d_{\psi})^{-\frac{1}{4}} (d_{\sigma} d_{\sigma} d_{\psi})^{-\frac{1}{3}} \begin{array}{c} \psi \quad \sigma \\ \sigma \quad \sigma \\ \sigma \quad \psi \end{array} = -2^{-\frac{1}{12}}. \end{aligned} \quad (\text{A2})$$

As for the strange correlator, we need to project physical legs to a direct product state

$$\langle \omega(\beta) | = \sqrt{2}(\cosh \beta \langle \mathbf{1} | + \sinh \beta \langle \psi |). \quad (\text{A3})$$

In order to follow the square lattice structure, we construct the tensor unit as an octagon containing 8 triangles:

$$A_{ijkl} = \begin{array}{c} i \\ \text{---} \\ \text{---} \\ \text{---} \\ \text{---} \\ \text{---} \\ \text{---} \\ \text{---} \\ k \end{array} \quad \begin{array}{c} j \\ \text{---} \\ \text{---} \\ \text{---} \\ \text{---} \\ \text{---} \\ \text{---} \\ \text{---} \\ l \end{array} \quad \text{where } i, j, k, l = \mathbf{1} \text{ or } \psi, \quad \begin{array}{|} \hline \\ \hline \end{array} = \sigma, \quad \begin{array}{|} \hline \hline \\ \hline \end{array} = \omega. \quad (\text{A4})$$

To calculate the value of A_{ijkl} , we first check each pair of 2 triangles:

$$\begin{array}{c} i \\ \text{---} \\ \text{---} \\ \text{---} \\ j \end{array} = \begin{array}{c} i \\ \text{---} \\ \text{---} \\ \text{---} \\ j \end{array} = \begin{cases} 2^{\frac{1}{3}}(\cosh \beta + \sinh \beta) = 2^{\frac{1}{3}}e^{\beta}, & (i, j) = (\mathbf{1}, \mathbf{1}) \text{ or } (\psi, \psi); \\ 2^{\frac{1}{3}}(\cosh \beta - \sinh \beta) = 2^{\frac{1}{3}}e^{-\beta}, & (i, j) = (\mathbf{1}, \psi) \text{ or } (\psi, \mathbf{1}). \end{cases} \quad (\text{A5})$$

Then clearly

$$A_{\mathbf{1}\mathbf{1}\mathbf{1}\mathbf{1}} = A_{\psi\psi\psi\psi} = 2^{\frac{4}{3}}e^{4\beta}, \quad A_{\mathbf{1}\psi\mathbf{1}\psi} = A_{\psi\mathbf{1}\psi\mathbf{1}} = 2^{\frac{4}{3}}e^{-4\beta}, \quad \text{others} = 2^{\frac{4}{3}}. \quad (\text{A6})$$

This is exactly the tensor representation of Ising interaction around a plaquette of spins:

$$A_{ijkl} := A_{\sigma_i\sigma_j\sigma_k\sigma_l} = e^{\beta(\sigma_i\sigma_j + \sigma_j\sigma_k + \sigma_k\sigma_l + \sigma_l\sigma_i)}, \quad (\text{A7})$$

up to some overall factor. Finally, we should mention that in this scheme, the critical temperature β_c can be given via shifting the octagon by 1/2 unit and employing the Kramers–Wannier duality.

Using the tensor network representation built from equations (A6) and (A7), the partition function of 2D critical Ising model can now be written as

$$Z = \sum_{\{\sigma\}} \prod_{\langle i, j \rangle} e^{\beta\sigma_i\sigma_j} = \lim_{m \rightarrow \infty} \text{Tr } M^m, \quad (\text{A8})$$

where M is the transfer matrix:

$$M_{k_1 k_2 \dots k_n}^{i_1 i_2 \dots i_n} = \sum_{j_1, j_2, \dots, j_n} \prod_{\alpha=1}^n A_{i_\alpha j_\alpha k_\alpha j_{\alpha+1}} = \begin{array}{c} i_1 \quad i_2 \quad i_3 \quad \dots \quad i_n \\ \text{---} \\ \text{---} \\ \text{---} \\ \text{---} \\ \text{---} \\ \text{---} \\ \text{---} \\ j_1 \quad j_2 \quad j_3 \quad \dots \quad j_n \\ \text{---} \\ k_1 \quad k_2 \quad k_3 \quad \dots \quad k_n \end{array}. \quad (\text{A9})$$

The Ising CFT spectrum can then be obtained by diagonalizing $T \cdot M$, where T is the translation operator (11). The spectrum data are listed in Table II, where “ ∞ ” column is extrapolated from the raw data, with the power-law formula $\Delta = An^{-k} + B$. We can visualize them in Figure 4.

Spin \ Size	4	8	12	16	20	24	∞	Exact
0	0.123499	0.124606	0.124823	0.124900	0.124936	0.124955	0.125005 (1)	$\frac{1}{8}$
0	1.026740	1.006488	1.002868	1.001610	1.001030	1.000715	1.00004 (1)	1
± 1	1.245699	1.151345	1.136446	1.131388	1.129074	1.127824	1.1257 (2)	$1 + \frac{1}{8}$
$\pm 1, \pm 2$	2.569513	2.098365	2.041544	2.022974	2.014590	2.010090	2.006 (2)	2
0	2.367899	2.178085	2.148069	2.137876	2.133212	2.130692	2.1265 (4)	$2 + \frac{1}{8}$
± 2	-	2.369005	2.223018	2.178379	2.158670	2.148201	2.1297 (9)	$2 + \frac{1}{8}$

TABLE II. Ising spectrum. The cylinder size is from 4 to 24 and is extrapolated to infinity, with data listed in the “ ∞ ” column.

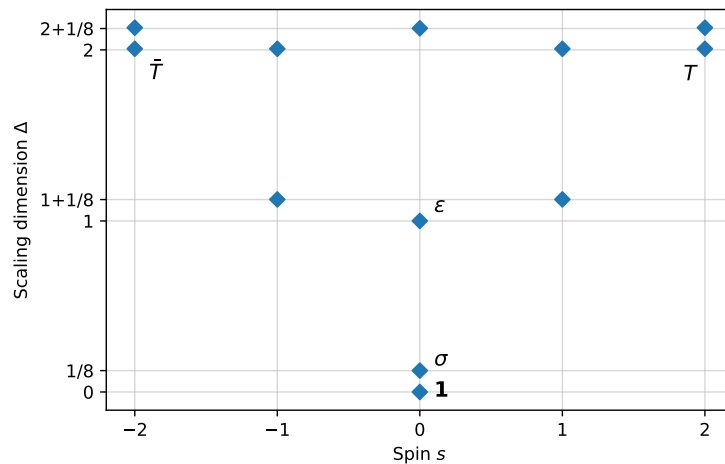


FIG. 4. Ising spectrum corresponding to the cylinder transfer matrix of size $n \rightarrow \infty$. Primary states are labeled with their corresponding operators in the CFT.

Appendix B: Implementation details

The implementation of the matrix-vector multiplication in the LinearOperator method is illustrated in [Figure 5](#). Since the transfer matrix M has already been written in a ring of A tensors, the multiplication $M \cdot v$ is then constructed by applying the tensor units iteratively. To obtain the translation operator equation [\(11\)](#), we can permute the elements of v by a simple array indexing operation. For the n -site cylinder with bond dimension χ , LinearOperator method can largely reduce the memory consumption from $\mathcal{O}(\chi^{2n})$ to $\mathcal{O}(\chi^n)$, which makes the calculation of large cylinders possible. We use the standard Arnoldi algorithm for the diagonalization of the transfer matrix, where the LinearOperator method can also apply.

Appendix C: Numerical details for the Virasoro operators

We check the validity of the lattice Virasoro operators (obtained from the cylinder eigenstates of size $n = 18$) by applying them to low-energy eigenstates of a coarse-grained lattice with cylinder size $N = 3$. The matrix elements $\langle \phi_\alpha | L_n | \phi_\beta \rangle$ for $n = \pm 1$ and ± 2 are listed in [Table III–VIII](#) and their behaviors on the conformal towers are illustrated in [Figure 6](#) and [7](#). In the tables, the matrix elements between states and their correct Virasoro descendants are highlighted in bold blue, whereas the erroneous matrix elements are marked in pale blue.

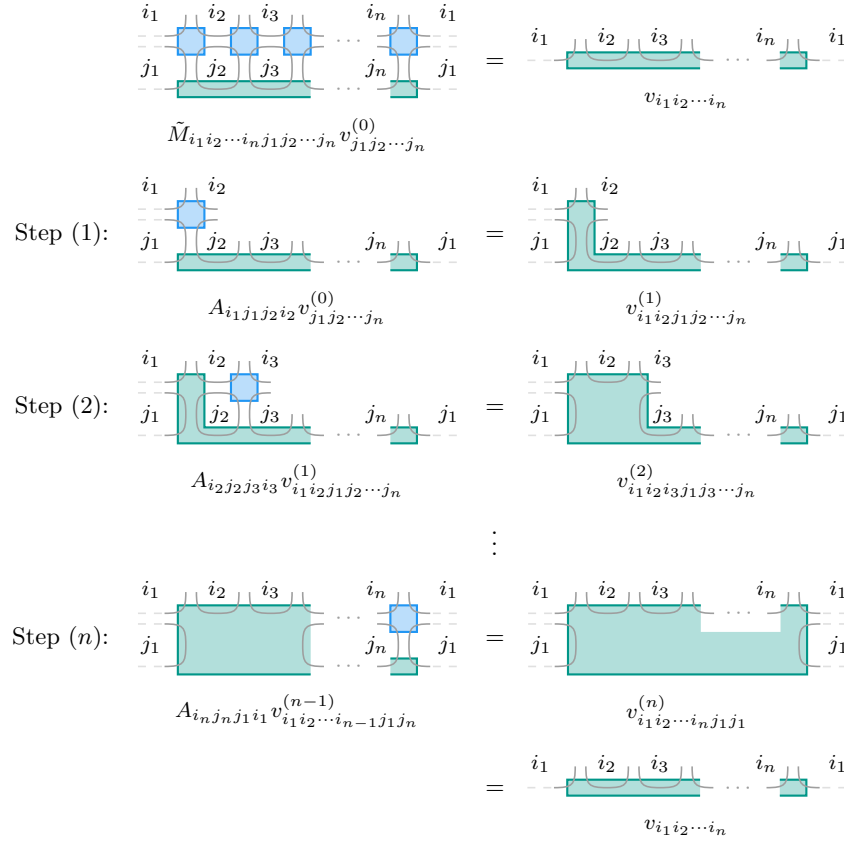


FIG. 5. Implementation of the matrix-vector multiplication $M \cdot v$ in the LinearOperator method for Fibonacci string-net.

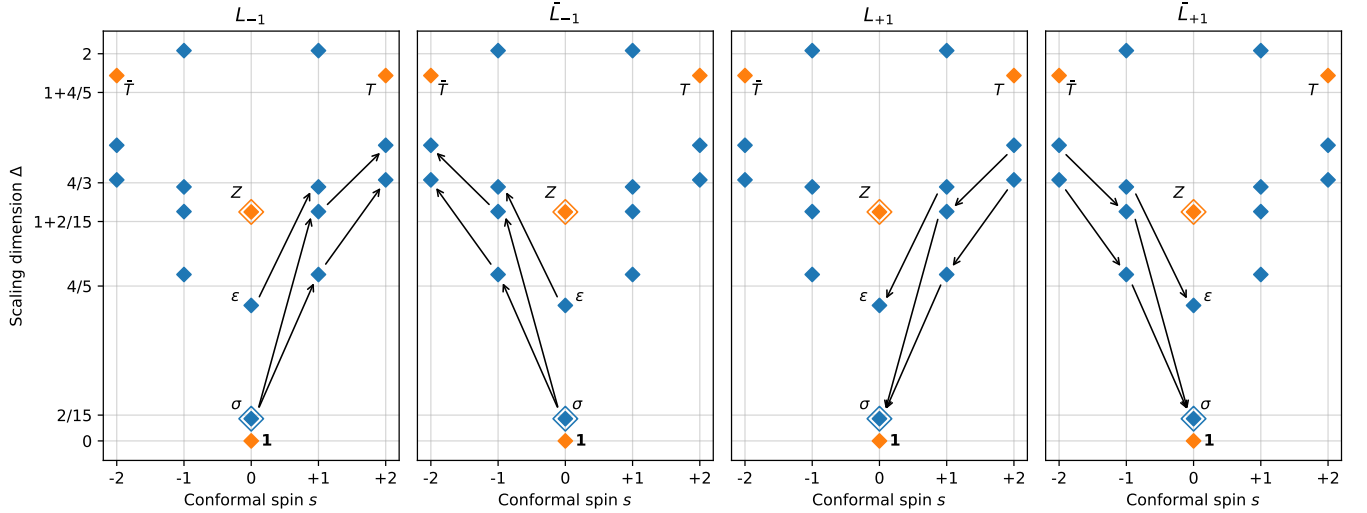


FIG. 6. Actions of lattice $L_{\pm 1}$ and $\bar{L}_{\pm 1}$ in the low-energy subspace of cylinder transfer matrix of size $N = 3$ and bond dimension $\chi = 64$. Corresponding matrix elements are listed in Table III–VI.

$ \phi_\alpha\rangle$	Δ_α	$\Delta_\alpha^{\text{exact}}$	s_α	$\langle\phi_\alpha L_{-1} 2\rangle$	$\langle\phi_\alpha L_{-1} 3\rangle$	$\langle\phi_\alpha L_{-1} 4\rangle$	$\langle\phi_\alpha L_{-1} 5\rangle$	$\langle\phi_\alpha L_{-1} 6\rangle$	$\langle\phi_\alpha L_{-1} 7\rangle$	$\langle\phi_\alpha L_{-1} 8\rangle$
1	0.000	0	0	1.668e-16	1.063e-16	2.449e-16	2.247e-16	1.924e-02	1.837e-16	1.297e-02
2	0.115	$\frac{2}{15}$	0	1.332e-16	1.264e-16	6.993e-17	1.013e-15	3.914e-02	1.133e-16	1.395e-01
3	0.115	$\frac{2}{15}$	0	2.676e-16	8.564e-17	9.721e-17	2.311e-16	1.436e-01	3.369e-16	3.779e-02
4	0.700	$\frac{4}{5}$	0	9.051e-16	9.529e-16	2.877e-16	8.961e-16	1.528e-01	4.405e-16	1.456e-01
5	1.185	$1+\frac{2}{15}$	+1	9.653e-01	9.059e-02	2.550e-02	4.998e-16	1.203e-16	1.033e-16	1.854e-16
6	0.860	$1+\frac{2}{15}$	-1	3.743e-15	1.485e-14	1.905e-15	3.670e-02	9.813e-16	5.692e-01	4.330e-16
7	0.860	$1+\frac{2}{15}$	+1	1.054e-01	9.112e-01	5.579e-02	6.870e-17	1.497e-16	2.763e-16	6.323e-16
8	1.185	$1+\frac{2}{15}$	-1	4.086e-14	5.837e-15	1.360e-15	8.688e-01	3.384e-16	1.440e-02	4.357e-15
9	1.183	$\frac{4}{3}$	0	1.408e-14	2.396e-15	1.321e-15	9.665e-16	6.665e-03	5.264e-16	2.095e-02
10	1.183	$\frac{4}{3}$	0	9.490e-15	2.714e-15	3.248e-16	1.626e-15	2.858e-03	2.244e-15	2.560e-02
11	1.312	$1+\frac{4}{5}$	+1	9.616e-02	2.486e-01	8.767e-01	3.467e-16	2.227e-16	7.391e-17	2.155e-16
12	1.312	$1+\frac{4}{5}$	-1	9.042e-16	3.220e-15	1.149e-14	2.295e-01	3.092e-16	2.371e-01	1.272e-15
13	1.887	2	+2	4.287e-16	1.287e-15	4.530e-15	9.052e-03	7.307e-16	7.514e-02	2.232e-16
14	1.887	2	-2	5.546e-02	3.241e-02	2.098e-01	1.801e-15	5.093e-16	1.742e-15	2.569e-15
15	1.527	$2+\frac{2}{15}$	+2	1.466e-15	1.605e-16	6.354e-16	2.863e-01	6.779e-16	1.974e-01	1.335e-15
16	1.348	$2+\frac{2}{15}$	-2	1.480e-03	6.605e-01	3.804e-01	1.088e-15	1.692e-16	4.408e-15	4.819e-16
17	1.348	$2+\frac{2}{15}$	+2	3.851e-16	5.451e-16	2.807e-16	9.368e-02	1.927e-15	9.331e-01	9.124e-16
18	1.527	$2+\frac{2}{15}$	-2	7.978e-03	2.011e-02	7.351e-01	3.228e-15	2.967e-16	1.856e-15	6.081e-16

TABLE III. $\langle\phi_\alpha|L_{-1}|\phi_\beta\rangle$

$ \phi_\alpha\rangle$	Δ_α	$\Delta_\alpha^{\text{exact}}$	s_α	$\langle\phi_\alpha \bar{L}_{-1} 2\rangle$	$\langle\phi_\alpha \bar{L}_{-1} 3\rangle$	$\langle\phi_\alpha \bar{L}_{-1} 4\rangle$	$\langle\phi_\alpha \bar{L}_{-1} 5\rangle$	$\langle\phi_\alpha \bar{L}_{-1} 6\rangle$	$\langle\phi_\alpha \bar{L}_{-1} 7\rangle$	$\langle\phi_\alpha \bar{L}_{-1} 8\rangle$
1	0.000	0	0	1.332e-16	1.782e-16	2.228e-16	1.297e-02	1.755e-16	1.924e-02	1.980e-16
2	0.115	$\frac{2}{15}$	0	6.331e-17	2.548e-16	8.701e-17	3.779e-02	3.451e-16	1.436e-01	2.382e-16
3	0.115	$\frac{2}{15}$	0	1.351e-16	1.343e-16	6.665e-17	1.395e-01	1.049e-16	3.914e-02	1.013e-15
4	0.700	$\frac{4}{5}$	0	9.563e-16	8.944e-16	2.835e-16	1.456e-01	4.352e-16	1.528e-01	8.986e-16
5	1.185	$1+\frac{2}{15}$	+1	5.836e-15	4.088e-14	1.342e-15	4.295e-15	1.440e-02	2.886e-16	8.688e-01
6	0.860	$1+\frac{2}{15}$	-1	9.112e-01	1.054e-01	5.579e-02	6.370e-16	2.610e-16	1.433e-16	8.604e-17
7	0.860	$1+\frac{2}{15}$	+1	1.489e-14	3.625e-15	1.958e-15	4.199e-16	5.692e-01	8.834e-16	3.670e-02
8	1.185	$1+\frac{2}{15}$	-1	9.059e-02	9.653e-01	2.550e-02	1.756e-16	1.109e-16	1.284e-16	5.018e-16
9	1.183	$\frac{4}{3}$	0	2.780e-15	9.422e-15	3.590e-16	2.560e-02	2.174e-15	2.858e-03	1.636e-15
10	1.183	$\frac{4}{3}$	0	2.363e-15	1.403e-14	1.313e-15	2.095e-02	5.253e-16	6.665e-03	9.721e-16
11	1.312	$1+\frac{4}{5}$	+1	3.269e-15	8.494e-16	1.152e-14	1.212e-15	2.371e-01	3.656e-16	2.295e-01
12	1.312	$1+\frac{4}{5}$	-1	2.486e-01	9.616e-02	8.767e-01	1.973e-16	7.044e-17	2.180e-16	3.385e-16
13	1.887	2	+2	3.241e-02	5.546e-02	2.098e-01	2.547e-15	1.751e-15	5.323e-16	1.771e-15
14	1.887	2	-2	1.216e-15	4.646e-16	4.497e-15	2.205e-16	7.514e-02	7.693e-16	9.052e-03
15	1.527	$2+\frac{2}{15}$	+2	2.011e-02	7.978e-03	7.351e-01	6.155e-16	1.839e-15	2.672e-16	3.215e-15
16	1.348	$2+\frac{2}{15}$	-2	5.333e-16	3.697e-16	2.794e-16	9.403e-16	9.331e-01	1.924e-15	9.368e-02
17	1.348	$2+\frac{2}{15}$	+2	6.605e-01	1.480e-03	3.804e-01	4.580e-16	4.341e-15	2.112e-16	1.088e-15
18	1.527	$2+\frac{2}{15}$	-2	1.368e-16	1.532e-15	6.654e-16	1.282e-15	1.974e-01	6.726e-16	2.863e-01

TABLE IV. $\langle\phi_\alpha|\bar{L}_{-1}|\phi_\beta\rangle$

$ \phi_\alpha\rangle$	Δ_α	$\Delta_\alpha^{\text{exact}}$	s_α	$\langle\phi_\alpha L_{+1} 5\rangle$	$\langle\phi_\alpha L_{+1} 6\rangle$	$\langle\phi_\alpha L_{+1} 7\rangle$	$\langle\phi_\alpha L_{+1} 8\rangle$	$\langle\phi_\alpha L_{+1} 11\rangle$	$\langle\phi_\alpha L_{+1} 12\rangle$	$\langle\phi_\alpha L_{+1} 15\rangle$	$\langle\phi_\alpha L_{+1} 17\rangle$
1	0.000	0	0	1.039e-01	2.787e-16	1.357e-01	5.910e-16	1.975e-02	6.362e-17	1.446e-16	7.152e-17
2	0.115	$\frac{2}{15}$	0	9.009e-01	5.282e-16	7.788e-02	4.695e-15	2.377e-02	1.748e-16	3.096e-16	2.613e-16
3	0.115	$\frac{2}{15}$	0	1.076e-01	1.699e-15	9.004e-01	8.795e-16	1.228e-02	1.804e-16	1.009e-16	2.888e-16
4	0.700	$\frac{4}{5}$	0	3.127e-02	9.127e-17	3.978e-02	4.922e-16	6.543e-01	1.632e-15	3.342e-16	3.956e-16
5	1.185	$1+\frac{2}{15}$	+1	1.093e-15	1.126e-02	3.602e-16	2.028e-01	4.985e-16	1.280e-01	2.043e-01	7.993e-02
6	0.860	$1+\frac{2}{15}$	-1	2.469e-16	7.992e-16	2.700e-16	3.027e-16	1.075e-16	3.936e-16	4.661e-16	5.142e-15
7	0.860	$1+\frac{2}{15}$	+1	4.036e-17	1.342e-01	4.806e-16	3.159e-03	1.523e-16	1.822e-02	1.384e-02	8.273e-01
8	1.185	$1+\frac{2}{15}$	-1	5.780e-16	2.047e-16	2.252e-15	2.400e-15	5.186e-16	1.352e-15	2.230e-15	1.923e-15
9	1.183	$\frac{4}{3}$	0	1.991e-02	2.422e-16	5.860e-04	9.291e-16	6.752e-02	5.515e-16	8.351e-16	5.743e-16
10	1.183	$\frac{4}{3}$	0	4.026e-02	8.613e-17	1.138e-02	5.202e-16	9.652e-02	2.857e-16	7.076e-16	9.802e-16
11	1.312	$1+\frac{4}{5}$	+1	8.062e-16	8.189e-02	4.240e-16	1.411e-01	2.285e-16	2.620e-02	5.288e-02	8.538e-02
12	1.312	$1+\frac{4}{5}$	-1	8.267e-17	2.347e-16	4.970e-16	3.741e-17	4.512e-16	1.381e-16	2.376e-16	5.710e-16
13	1.887	2	+2	2.734e-16	2.423e-16	5.158e-17	1.735e-16	1.009e-16	2.237e-16	1.145e-16	8.372e-17
14	1.887	2	-2	1.707e-15	1.140e-01	1.772e-15	5.354e-02	1.110e-15	5.932e-02	6.955e-02	8.001e-02
15	1.527	$2+\frac{2}{15}$	+2	9.009e-16	1.473e-16	8.538e-17	2.064e-16	4.773e-17	1.280e-16	6.262e-17	9.921e-17
16	1.348	$2+\frac{2}{15}$	-2	1.737e-15	1.919e-01	9.190e-16	3.725e-03	4.467e-16	1.090e-01	2.726e-01	4.972e-01
17	1.348	$2+\frac{2}{15}$	+2	4.061e-17	1.464e-16	3.346e-16	4.723e-16	1.234e-16	1.344e-16	1.100e-16	4.950e-16
18	1.527	$2+\frac{2}{15}$	-2	3.148e-16	5.491e-01	1.778e-15	6.810e-02	2.825e-16	9.379e-02	1.075e-02	3.427e-01

TABLE V. $\langle\phi_\alpha|L_{+1}|\phi_\beta\rangle$

$ \phi_\alpha\rangle$	Δ_α	$\Delta_\alpha^{\text{exact}}$	s_α	$\langle\phi_\alpha \bar{L}_{+1} 5\rangle$	$\langle\phi_\alpha \bar{L}_{+1} 6\rangle$	$\langle\phi_\alpha \bar{L}_{+1} 7\rangle$	$\langle\phi_\alpha \bar{L}_{+1} 8\rangle$	$\langle\phi_\alpha \bar{L}_{+1} 11\rangle$	$\langle\phi_\alpha \bar{L}_{+1} 12\rangle$	$\langle\phi_\alpha \bar{L}_{+1} 16\rangle$	$\langle\phi_\alpha \bar{L}_{+1} 18\rangle$
1	0.000	0	0	5.855e-16	1.357e-01	2.693e-16	1.039e-01	8.166e-17	1.975e-02	1.041e-16	1.189e-16
2	0.115	$\frac{2}{15}$	0	9.024e-16	9.004e-01	1.656e-15	1.076e-01	1.928e-16	1.228e-02	2.915e-16	1.348e-16
3	0.115	$\frac{2}{15}$	0	4.735e-15	7.788e-02	5.232e-16	9.009e-01	1.782e-16	2.377e-02	2.380e-16	3.062e-16
4	0.700	$\frac{4}{5}$	0	5.104e-16	3.978e-02	1.032e-16	3.127e-02	1.610e-15	6.543e-01	3.864e-16	3.288e-16
5	1.185	$1+\frac{2}{15}$	+1	2.385e-15	2.248e-15	2.051e-16	5.693e-16	1.353e-15	5.051e-16	1.939e-15	2.248e-15
6	0.860	$1+\frac{2}{15}$	-1	3.159e-03	4.519e-16	1.342e-01	4.389e-17	1.822e-02	1.569e-16	8.273e-01	1.384e-02
7	0.860	$1+\frac{2}{15}$	+1	3.099e-16	2.725e-16	8.148e-16	2.299e-16	3.277e-16	1.078e-16	5.155e-15	4.757e-16
8	1.185	$1+\frac{2}{15}$	-1	2.028e-01	3.572e-16	1.126e-02	1.066e-15	1.280e-01	4.561e-16	7.993e-02	2.043e-01
9	1.183	$\frac{4}{3}$	0	4.994e-16	1.138e-02	6.255e-17	4.026e-02	2.829e-16	9.652e-02	9.567e-16	6.775e-16
10	1.183	$\frac{4}{3}$	0	9.015e-16	5.860e-04	2.327e-16	1.991e-02	5.194e-16	6.752e-02	5.520e-16	8.260e-16
11	1.312	$1+\frac{4}{5}$	+1	4.673e-17	4.944e-16	2.249e-16	8.800e-17	1.418e-16	4.762e-16	5.909e-16	2.370e-16
12	1.312	$1+\frac{4}{5}$	-1	1.411e-01	4.286e-16	8.189e-02	8.016e-16	2.620e-02	2.180e-16	8.538e-02	5.288e-02
13	1.887	2	+2	5.354e-02	1.809e-15	1.140e-01	1.732e-15	5.932e-02	1.075e-15	8.001e-02	6.955e-02
14	1.887	2	-2	1.717e-16	7.352e-17	2.281e-16	3.081e-16	2.331e-16	1.036e-16	7.397e-17	1.289e-16
15	1.527	$2+\frac{2}{15}$	+2	6.810e-02	1.882e-15	5.491e-01	3.442e-16	9.379e-02	3.299e-16	3.427e-01	1.075e-02
16	1.348	$2+\frac{2}{15}$	-2	4.734e-16	3.378e-16	1.229e-16	1.980e-17	1.401e-16	1.297e-16	5.183e-16	1.179e-16
17	1.348	$2+\frac{2}{15}$	+2	3.725e-03	9.342e-16	1.919e-01	1.768e-15	1.090e-01	4.343e-16	4.972e-01	2.726e-01
18	1.527	$2+\frac{2}{15}$	-2	1.846e-16	7.373e-17	1.417e-16	8.890e-16	1.367e-16	2.964e-17	8.957e-17	6.303e-17

TABLE VI. $\langle\phi_\alpha|\bar{L}_{+1}|\phi_\beta\rangle$

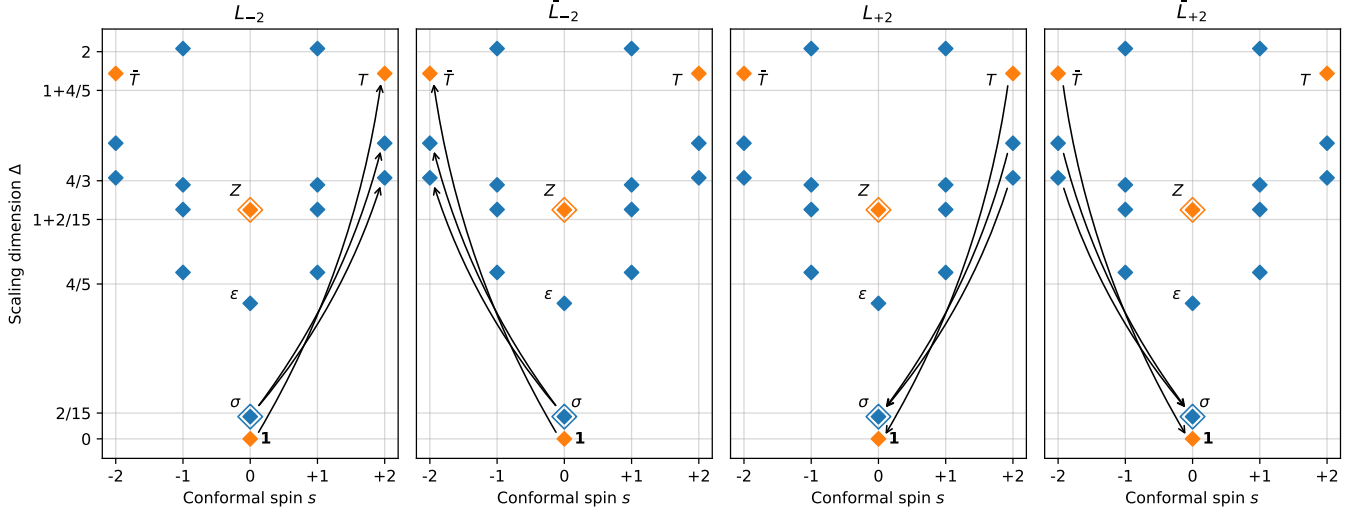


FIG. 7. Actions of lattice $L_{\pm 2}$ and $\bar{L}_{\pm 2}$ in the low-energy subspace of cylinder transfer matrix of size $N = 3$ and bond dimension $\chi = 64$. Corresponding matrix elements are listed in Table VII and VIII.

$ \phi_\alpha\rangle$	Δ_α	$\Delta_\alpha^{\text{exact}}$	s_α	$\langle\phi_\alpha L_{-2} 1\rangle$	$\langle\phi_\alpha L_{-2} 2\rangle$	$\langle\phi_\alpha L_{-2} 3\rangle$	$\langle\phi_\alpha \bar{L}_{-2} 1\rangle$	$\langle\phi_\alpha \bar{L}_{-2} 2\rangle$	$\langle\phi_\alpha \bar{L}_{-2} 3\rangle$
1	0.000	0	0	5.070e-16	4.120e-16	5.410e-17	4.914e-16	4.335e-17	3.879e-16
2	0.115	$\frac{2}{15}$	0	2.123e-16	2.762e-16	1.842e-16	1.521e-16	9.780e-17	1.980e-16
3	0.115	$\frac{2}{15}$	0	9.160e-17	1.961e-16	7.979e-17	2.055e-16	1.908e-16	2.668e-16
4	0.700	$\frac{4}{5}$	0	1.860e-16	2.123e-16	3.320e-16	1.826e-16	3.088e-16	2.244e-16
5	1.185	$1+\frac{2}{15}$	+1	4.027e-16	1.686e-15	6.714e-16	8.983e-02	1.722e-01	8.496e-01
6	0.860	$1+\frac{2}{15}$	-1	7.056e-02	1.513e-01	5.550e-01	7.152e-17	5.173e-16	1.546e-16
7	0.860	$1+\frac{2}{15}$	+1	9.127e-17	1.621e-16	5.064e-16	7.056e-02	5.550e-01	1.513e-01
8	1.185	$1+\frac{2}{15}$	-1	8.983e-02	8.496e-01	1.722e-01	4.163e-16	6.801e-16	1.651e-15
9	1.183	$\frac{4}{3}$	0	3.034e-16	1.516e-15	4.880e-16	1.413e-16	1.837e-15	1.510e-15
10	1.183	$\frac{4}{3}$	0	1.355e-16	1.478e-15	1.836e-15	3.118e-16	5.225e-16	1.521e-15
11	1.312	$1+\frac{4}{5}$	+1	8.784e-17	9.239e-16	3.474e-16	1.213e-01	1.645e-01	5.981e-01
12	1.312	$1+\frac{4}{5}$	-1	1.213e-01	5.981e-01	1.645e-01	1.110e-16	3.210e-16	9.200e-16
13	1.887	2	+2	9.866e-01	6.101e-02	6.156e-02	5.115e-14	6.659e-15	5.855e-15
14	1.887	2	-2	5.103e-14	5.967e-15	6.529e-15	9.866e-01	6.156e-02	6.101e-02
15	1.527	$2+\frac{2}{15}$	+2	1.242e-01	9.650e-01	8.627e-03	7.442e-15	1.471e-15	5.853e-14
16	1.348	$2+\frac{2}{15}$	-2	1.741e-15	2.444e-15	7.129e-15	5.512e-02	9.282e-01	1.594e-01
17	1.348	$2+\frac{2}{15}$	+2	5.512e-02	1.594e-01	9.282e-01	1.791e-15	7.104e-15	2.544e-15
18	1.527	$2+\frac{2}{15}$	-2	7.514e-15	5.851e-14	1.378e-15	1.242e-01	8.627e-03	9.650e-01

TABLE VII. $\langle\phi_\alpha|L_{-2}|\phi_\beta\rangle$ and $\langle\phi_\alpha|\bar{L}_{-2}|\phi_\beta\rangle$

$ \phi_\alpha\rangle$	Δ_α	$\Delta_\alpha^{\text{exact}}$	s_α	$\langle\phi_\alpha L_{+2} 13\rangle$	$\langle\phi_\alpha L_{+2} 14\rangle$	$\langle\phi_\alpha L_{+2} 15\rangle$	$\langle\phi_\alpha L_{+2} 17\rangle$	$\langle\phi_\alpha \bar{L}_{+2} 13\rangle$	$\langle\phi_\alpha \bar{L}_{+2} 14\rangle$	$\langle\phi_\alpha \bar{L}_{+2} 16\rangle$	$\langle\phi_\alpha \bar{L}_{+2} 18\rangle$
1	0.000	0	0	8.968e-01	1.644e-15	7.211e-02	4.644e-02	1.590e-15	8.968e-01	4.644e-02	7.211e-02
2	0.115	$\frac{2}{15}$	0	6.005e-02	4.075e-16	7.117e-01	9.349e-02	1.876e-16	3.489e-02	7.512e-01	2.103e-02
3	0.115	$\frac{2}{15}$	0	3.489e-02	1.714e-16	2.103e-02	7.512e-01	3.855e-16	6.005e-02	9.349e-02	7.117e-01
4	0.700	$\frac{4}{5}$	0	4.257e-03	1.786e-16	3.160e-02	2.784e-02	1.794e-16	4.257e-03	2.784e-02	3.160e-02
5	1.185	$1+\frac{2}{15}$	+1	1.357e-16	2.602e-16	2.121e-16	5.904e-17	2.340e-02	4.367e-16	2.207e-15	4.641e-16
6	0.860	$1+\frac{2}{15}$	-1	3.538e-16	2.998e-02	3.029e-16	3.710e-16	1.428e-16	4.351e-17	3.006e-16	1.212e-16
7	0.860	$1+\frac{2}{15}$	+1	3.852e-17	1.425e-16	1.114e-16	3.006e-16	2.998e-02	3.067e-16	4.008e-16	3.221e-16
8	1.185	$1+\frac{2}{15}$	-1	3.408e-16	2.340e-02	4.807e-16	2.198e-15	2.494e-16	1.399e-16	6.533e-17	2.065e-16
9	1.183	$\frac{4}{3}$	0	9.324e-02	1.388e-16	2.006e-02	3.345e-02	2.233e-16	7.031e-02	1.587e-02	5.714e-02
10	1.183	$\frac{4}{3}$	0	7.031e-02	2.239e-16	5.714e-02	1.587e-02	1.457e-16	9.324e-02	3.345e-02	2.006e-02
11	1.312	$1+\frac{4}{5}$	+1	1.082e-16	2.425e-16	1.205e-16	5.608e-17	5.229e-02	4.634e-16	3.855e-16	7.252e-16
12	1.312	$1+\frac{4}{5}$	-1	4.306e-16	5.229e-02	6.871e-16	3.659e-16	2.526e-16	1.292e-16	7.423e-17	1.092e-16
13	1.887	2	+2	8.511e-16	1.922e-01	8.115e-16	2.390e-16	4.318e-16	5.357e-16	1.021e-15	5.484e-16
14	1.887	2	-2	5.592e-16	4.027e-16	5.619e-16	1.017e-15	1.922e-01	8.719e-16	2.616e-16	8.621e-16
15	1.527	$2+\frac{2}{15}$	+2	3.370e-16	3.141e-02	7.219e-16	1.422e-16	6.289e-16	7.121e-16	4.933e-16	4.516e-16
16	1.348	$2+\frac{2}{15}$	-2	6.436e-16	4.340e-17	8.115e-16	4.521e-16	7.064e-03	1.821e-16	5.489e-16	1.304e-16
17	1.348	$2+\frac{2}{15}$	+2	1.885e-16	7.064e-03	1.416e-16	5.210e-16	4.910e-17	6.729e-16	4.473e-16	7.427e-16
18	1.527	$2+\frac{2}{15}$	-2	7.152e-16	6.147e-16	4.650e-16	4.886e-16	3.141e-02	3.314e-16	1.340e-16	7.226e-16

TABLE VIII. $\langle\phi_\alpha|L_{+2}|\phi_\beta\rangle$ and $\langle\phi_\alpha|\bar{L}_{+2}|\phi_\beta\rangle$